Nanoscale

ROYAL SOCIETY
OF CHEMISTRY

PAPER
Ho Cheung Shum *et al.*
Co-doping optimized hydrogel-elastomer micro-actuators
for versatile biomimetic motions

NCNST

Check for updates

Co-doping optimized hydrogel-elastomer micro-actuators for versatile biomimetic motions†

Yi Pan, [ID] Lik Ho Lee, Zhenyu Yang, Sammer Ul Hassan and Ho Cheung Shum [ID] *

Hydrogels can respond to changes in humidity or temperature, while elastomers can resist structural collapse due to dehydration or external force application. A hybrid bilayer of hydrogel-elastomers while retaining the merits of both the hydrogels and elastomers has emerged as a promising stimuli-responsive micro-actuator. However, the preparation of a hydrogel-elastomer micro-actuator requires multiple steps, mainly due to the differences in the surface properties of these two materials. Among them, the steps to surface-treat the elastomer and functionalize the material of each layer involve intricate processes and excessive consumption of resources. In this work, we introduce a co-doping method to optimize the preparation of a stimuli-responsive hydrogel-elastomer micro-actuator. The surface treatment and functionalization processes are combined into one step by directly doping the polymerization initiator and functional nanomaterials into the hybrid bilayer. The thermo-responsive hydrogel is combined with a photothermal elastomer to fabricate a soft micro-actuator that can bend and unbend in response to changes in humidity and light. Based on this actuator, a set of biomimetic soft micro-robots were developed, demonstrating a series of motions, such as grabbing, crawling, and jumping. This strategy of stimuli-responsive micro-actuator preparation can benefit the hydrogel-elastomer hybrid micro-robot designs for applications ranging from self-locomotive robots in environmental monitoring to drug delivery in biomedical engineering.

Introduction

Small creatures in nature have evolved many unique ways of motion to adapt to their living environments. These have inspired scientists to design soft micro-robots.[1–5] For example, learning from the skimming motion of dragonflies over water surfaces, a smart soft robot was designed to monitor the water quality in ponds.[6] Tasks, such as object manipulation and navigation through tortuous paths, often require multiple co-ordinated motions, such as grabbing, crawling, and jumping.[7,8] While the motion of a macro-sized soft robot relies on the mechanical and structural design of the actuator, the motion of a soft micro-robot primarily depends on the stimuli-responsive materials that make up the micro-actuator.[9] These soft micro-actuators are typically made of hydrogels, shape-memory polymers, and liquid crystal elastomers.[2,7,10,11] Among them, stimuli-responsive hydrogels are widely used because they are readily available and easier to process than other materials.[2,10,12–14] However, these hydrogels predominantly contain water with a content of 60–90 wt%, leading to

their liquid-like characteristics.[15] Water can transfer in and out of the polymer network of hydrogels, making them easily deformable. The lack of tougher supporting materials often results in structural collapse of the micro-actuator upon external force loading or excessive water loss during out-of-water operations.[15–17] Such properties of hydrogels restrict the scope of application for all-hydrogel-based actuators. Natural mammalian skins combine tough epidermis and soft dermis into hybrids with stronger interfaces between them. Inspired by the skin, elastomers have been combined with hydrogels to form a hydrogel-elastomer bilayer structure. Such type of hybrid bilayer structure maintains the inherent properties of the hydrogel while it is mechanically strengthened by the elastomer.[18–20] Besides, water-free elastomers can act as a skeleton to support the actuator structure, even when exposed to air for a prolonged period of time.

The hybrid bilayer enables the hydrogel and elastomer with different properties to complement each other, but the two materials are incompatible and require additional processing to combine them.[19,21,22] First, to graft hydrogel polymers onto elastomeric surfaces, the hydrogels typically have to go through free radical polymerization and surface covalent cross-linking. However, elastomers are highly permeable to oxygen, which severely inhibits these processes.[18] Second, the hydrophobicity of elastomeric surfaces also prevents the stable

Department of Mechanical Engineering, The University of Hong Kong, Pokfulam Road, Hong Kong, China. E-mail: ashum@hku.hk

adhesion of hydrophilic hydrogels.[19] The existing solutions to such issues are broadly classified into physical and chemical adhesion. Using a porous fabric as an interlayer, the prepolymer solutions of these two materials can sequentially fill in and cross-link both sides of the fabric, thereby physically interlocking the hydrogel and elastomer together. However, these interlayers will add a certain thickness to the bilayer structure that eventually prevents the hybrid bilayer thickness from reaching the micron-level.[19] Chemically, bilayers at the micron level can be formed by chemical linkage, but it involves various elastomer pre-treatments, such as plasma activation, spray coating, and reagent soaking.[21,23,24] Besides combining the hydrogel and elastomer, the resulting hybrid bilayer also needs to be functionalized.

To enable the operation of these micro-actuators, the material must respond to external stimuli, such as humidity, temperature, magnetism, and light, which determine how the actuator can be controlled. For instance, controlling an actuator made up of a thermo-responsive hydrogel will be inefficient in air due to the slow conductance of heat. To enhance the responsiveness and control in air, the thermo-responsive actuator could be functionalized photothermally to allow its control by light. Thus, the functionalization of materials provides various single-mechanism or hybrid control modes for the hydrogel-elastomer actuators. Consequently, the bonding challenges and requirements for functionalization inevitably demand multiple processing steps.[19,20,23,25] Each process incurs cost, processing time, effort, and environmental impact, and often increases the failure rate. Hence, the preparation becomes detrimental to the fabrication efficiency and environmental sustainability, especially in mass production.[26] Therefore, a method with a concise process for surface treatment and material functionalization is required to prepare hydrogel-elastomer micro-actuators.

Doping is an approach to modifying material properties and has been applied to different materials, including nano and bulk materials. It introduces additional functionalities

without compromising the other desirable characteristics of the doped material. The co-doping of multiple dopants will add different functionalities to one system without causing interference between them. This co-doping approach is expected to combine material's surface pre-treatment and functionalization steps. For example, benzophenone (BP) is an oxygen inhibitor as well as a photoinitiator for free radical polymerization. It has been previously used to activate elastomeric surfaces for bonding with hydrogels.[18,20,27,28] Nanomaterials are also often employed in functionalizing elastomers to impart properties, such as photothermal and paramagnetic properties. In our study, we co-doped BP and functional nanomaterials directly into the system to combine multi-step pre-treatment and functionalization into a single step. As a demonstration, a hydrogel-elastomer micro-actuator is composed of a thermo-responsive poly(N-isopropylacrylamide) hydrogel (pNIPAM) and photothermal graphene nanoplatelet (GNP) doped polydimethylsiloxane elastomer (GPDMS). In this pNIPAM and GPDMS hybrid actuator (pNIPAM@GPDMS), the pNIPAM is the active layer that can swell or shrink in response to hydration and dehydration. The GPDMS is the mechanically inert layer to which GNPs are added to improve the photothermal properties. The resulting actuator shows an asymmetric response under humidity and light irradiation changes, leading to its bending or unbending structures, as shown in Fig. 1. Combined with the geometric design of the micro-actuator, some sophisticated motions can be derived from the bending and unbending movements. In this work, we developed a series of biomimetic soft micro-robots and demonstrated different motions, such as grabbing, crawling, and jumping. The successful implementation of these versatile biomimetic motions suggests that co-doping conveniently enhances the performance of hydrogel-elastomer micro-actuators. The co-doping approach for designing soft micro-robots could be further utilized in future environmental monitoring and biomedical engineering applications.
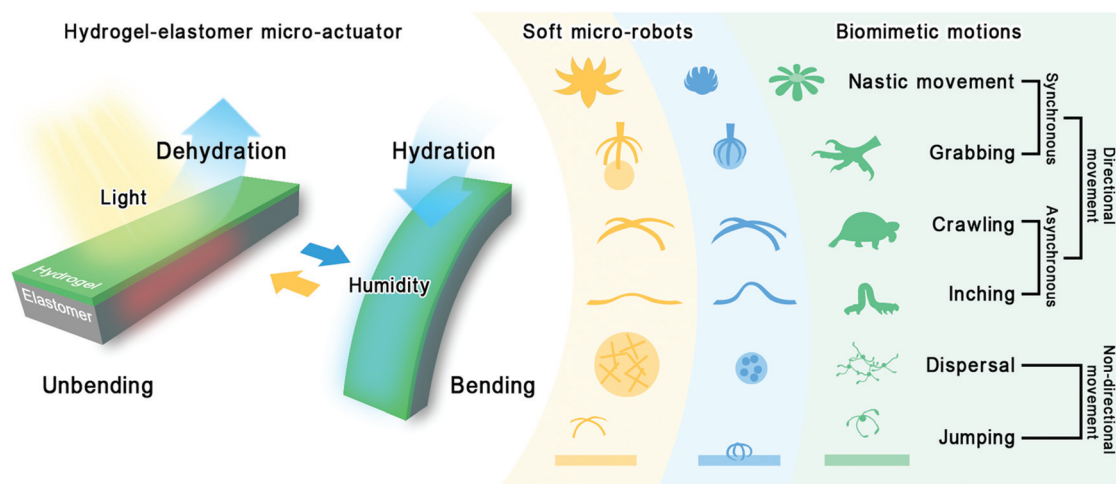

Fig. 1 Schematic illustration of the humidity- and light-responsive hydrogel–elastomer micro-actuator, the designed soft micro-robots, and their corresponding biomimetic motions.

Results and discussion

Preparation and characterization of the pNIPAM@GPDMS actuator

The humidity- and light-responsive hydrogel-elastomer bilayer actuators are prepared by chemically grafting a layer of the thermal responsive hydrogel pNIPAM onto the surface of the photothermal elastomer GPDMS (Fig. 2A). This is achieved by first mixing a BP solution and graphene nanoplatelets (GNPs) with PDMS precursors. BP functions as an oxygen inhibitor and a UV-triggered initiator for radical polymerization, while GNPs act as a photothermal conversion agent. The GPDMS is then coated and heat-cured on a flat substrate. Subsequently, a NIPAM monomer with a cross-linker is applied on the GPDMS surface, followed by UV treatment that excited the doped BP to its triplet state. The excited BP can abstract a hydrogen atom from the methyl group of PDMS to generate radicals capable of initiating the graft polymerization of NIPAM. Thereafter, a thin layer of pNIPAM is grafted onto the GPDMS to form a pNIPAM@GPDMS bilayer. The prepared pNIPAM@GPDMS bilayer could be easily cut into the desired shapes and peeled off from the substrate to form the designed soft micro-robot. The proposed method does not rely on any particular nano-materials. As long as the nanomaterial can be dispersed into
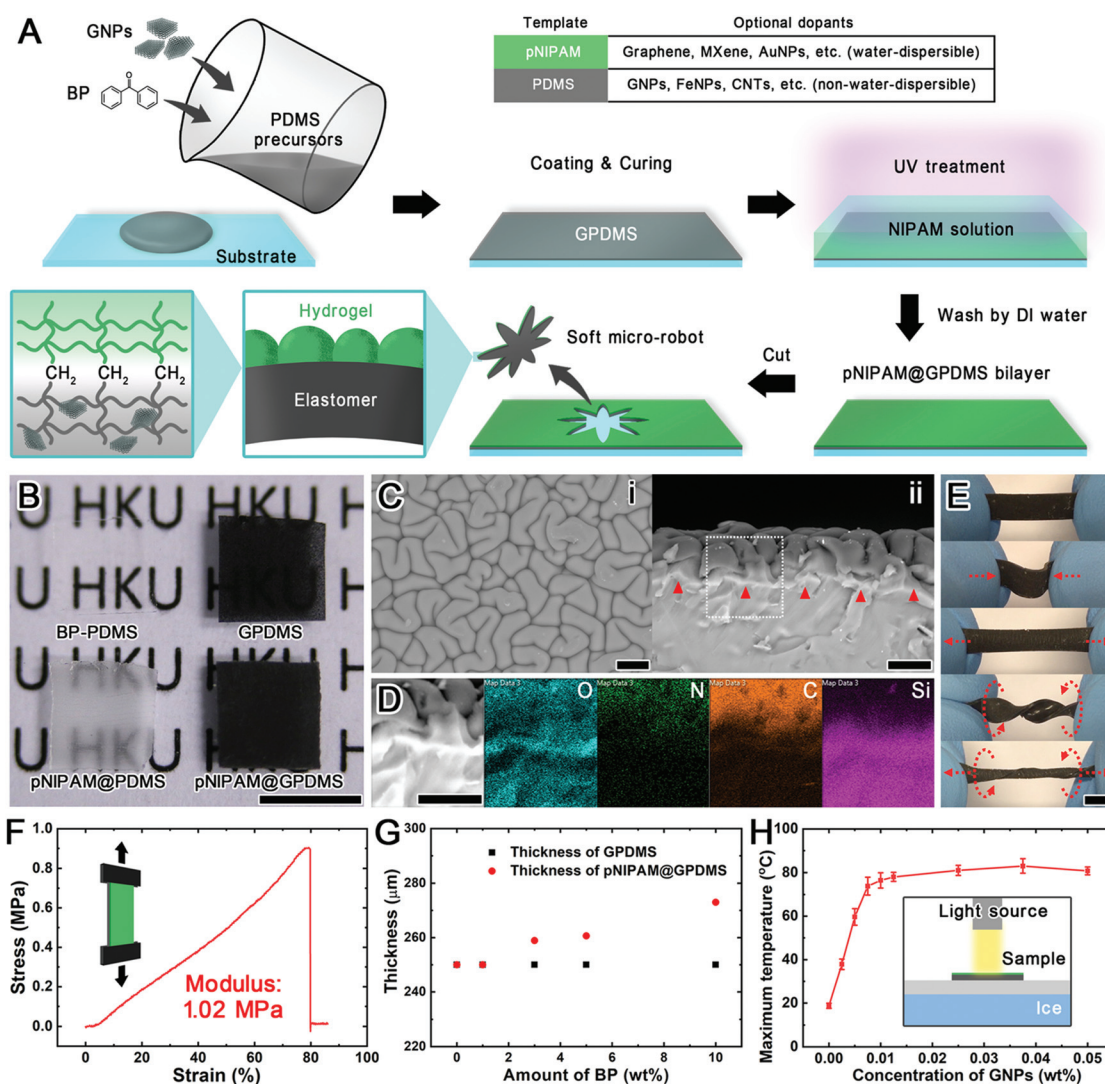

Fig. 2 Fabrication and characterization of the pNIPAM@GPDMS actuator. (A) Fabrication procedure of the pNIPAM@GPDMS actuator. Inset table: The options for dopants of each layer in the pNIPAM@PDMS template. (B) Photographs of different composites, including BP-PDMS, GPDMS, pNIPAM@PDMS, and pNIPAM@GPDMS. Scale bar: 5 mm. (C) SEM images: (i) top view of the pNIPAM layer and (ii) cross-section with an interface (marked with red arrows). (D) EDX mapping for the region in the dotted box in (Cii). Scale bars: 10 μm. (E) Photographs of the pNIPAM@GPDMS actuator before and after slackening, stretching, twisting, and twisted stretching. Scale bar: 5 mm. (F) Tensile test of the pNIPAM@GPDMS stripe. (G) Thickness of the pNIPAM layer *versus* the amount of BP applied in GPDMS. (H) The photothermal temperature increases with increasing concentration of doped GNPs in the pNIPAM@GPDMS samples. Thickness ≈ 400 μm. Irradiation time = 60 s. Power = 400 mW. Inset: Set-up a schematic of photothermal testing.

the NIPAM solution or PDMS precursors, it can be applied to the pNIPAM@PDMS template. Hence, various commonly used functional nanomaterials can be considered as doping candidates. To demonstrate its flexibility in the choice of dopants, we produced bilayers with water-dispersible dopants in pNIPAM such as carboxyl graphene, small diameter $Ti_3C_2T_x$ (MXene) thin layer, and gold nanoparticles (AuNPs) (Fig. S1†). In addition, non-water-dispersible dopants in PDMS such as GNPs, Fe_3O_4 nanoparticles (FeNPs), and carbon nanotubes (CNTs) were also prepared. These functional nanomaterials possess unique optical, electrical, and magnetic responsiveness, bringing more distinctive functions to the pNIPAM@PDMS bilayer system.

The BP doped PDMS (BP-PDMS) is transparent and similar to pure PDMS in appearance (Fig. 2B), while the GPDMS shows a dark black appearance, as GNPs have full-spectrum absorption and can be uniformly dispersed in PDMS (Fig. S2†). This class of graphene-based materials can exhibit plasmonic effects at specific wavelengths and generate heat through plasmonic photothermal conversion.[29–31] Thus, the GNP doped elastomer, GPDMS, shows a photothermal effect (Fig. S3†). This GPDMS achieves a temperature increase of about 83% within 20 s of visible light irradiation (400 mW). It can reach the maximum temperature after 1 min of irradiation and revert to ambient temperature after irradiation withdrawal within 1 min. Its photothermal responsiveness remains robust after hundreds of cycles of repeated light exposure. After modifying PDMS with the pNIPAM layer, the background beneath pNIPAM@PDMS becomes blurred (Fig. 2B). Also, pNIPAM@GPDMS is slightly paler than the unmodified GPDMS. Under scanning electron microscopy (SEM), wrinkles of pNIPAM are observed, indicating light scattering by the uneven hydrogel surfaces on the pNIPAM modified samples (Fig. 2Ci). These wrinkles result from the surface instability of the swelling hydrogel constrained by the unswollen PDMS.[32] The interface is clearly evident in the material cross-section (Fig. 2Cii and S4†) under both SEM and fluorescence microscopy. To further verify the chemical composition of the pNIPAM@GPDMS hybrid, we performed energy-dispersive X-ray spectroscopy (EDX) on a cross-section of the bilayer to detect oxygen- (O), nitrogen- (N), carbon- (C), and silicon (Si) regions of the specimen (Fig. 2D). The O signal is observed in the entire bilayer structure and is mainly derived from the carbonyl in pNIPAM and the siloxane backbone. However, apparent N and C signals can only be found on the top layer because N exists only in pNIPAM, and the carbon-rich GNPs are embedded inside the PDMS that EDX cannot detect. As the most abundant element in siloxane, Si can be easily detected on the GPDMS layer. These elemental analysis results prove the combination of pNIPAM and GPDMS layers. According to the literature on BP-assisted hydrogel-elastomer adhesion, these two layers bind to each other through covalent bonding.[18,28] Thus, they hardly detach from repeated deformation caused by external forces, such as slackening, stretching, twisting, and twisted stretching (Fig. 2E). It could even achieve a maximum tensile stress of 0.9 MPa with an elonga-

tion of about 80% (Young's modulus: 1.02 MPa) (Fig. 2F). These results show that the pNIPAM@GPDMS bilayer can withstand a certain degree of deformation caused by externally loaded forces. Its robust structure also provides mechanical support for the actuator to operate in a non-aqueous working environment.

With the co-doping method, the amount of the dopants can be easily adjusted, thus offering additional functions to the modified material and allowing customizable properties by varying the dosage of dopants used in the design. In our case, BP functions as an oxygen inhibitor as well as a polymerization initiator. A higher BP amount will favor the NIPAM polymerization reaction. The thickness of the pNIPAM layer would reflect the degree of its photopolymerization on the elastomeric surface. Thus, by gradually increasing the proportion of BP doped from 0 to 10 wt%, the thickness of the pNIPAM layer increases from 0 to 22 μm (Fig. 2G). This effect also enables adjusting the reaction time to obtain different thicknesses of the pNIPAM layers (Fig. S5B†). Together with the control of GPDMS thickness by spin coating speed (Fig. S5A†), the thickness of the two layers in the pNIPAM@GPDMS actuator can be deliberately tailored to meet the subsequent responsiveness requirements. Besides the adjustable thicknesses of the bilayer structure, additional functions in the bilayer could also be tuned by changing the amount of the functional dopants; for instance, changing the concentration of GNPs in PDMS allows the regulation of photothermal effects in GPDMS. The resulting GPDMS samples show different grayness in appearance (Fig. S2C†). As confirmed by the micrographs in Fig. S2,† GNPs are uniformly distributed in PDMS and the transmittance of the sample decreases with increasing concentrations of GNP doping. After modification with the pNIPAM layer, the photothermal responsiveness of the samples is tested under the same light irradiation conditions (Fig. 2H). The concentration of the doping GNPs between 0 and 0.01 wt% is found to vary linearly with the generated temperatures. A sample with 0.025 wt% GNP content even allows it to reach the highest temperature of 80 °C on an iced platform. Thus, the GPDMS can show a tunable photothermal effect through the dosage of GNPs. This tunable performance of the function in the bilayer further allows the stimuli-responsiveness of the prepared micro-actuator to be adjusted.

Stimuli-responsive bending and unbending of the pNIPAM@GPDMS actuator

The working principle of the bilayer actuator is based on the variations in swelling or shrinking between the two layers in response to stimuli. The swelling or shrinking of both layers is constrained by each other. Consequently, one layer is subjected to tension while the other is under compressive stress, resulting in bending motion to release internal stresses.[12] In our pNIPAM@GPDMS actuator, the pNIPAM layer mechanically functions as the active layer, while the GPDMS layer acts as the passive layer (Fig. 3A). The pNIPAM layer is a thermoresponsive hydrogel that can experience a coil-to-globule transition at temperatures higher than its lower critical solution
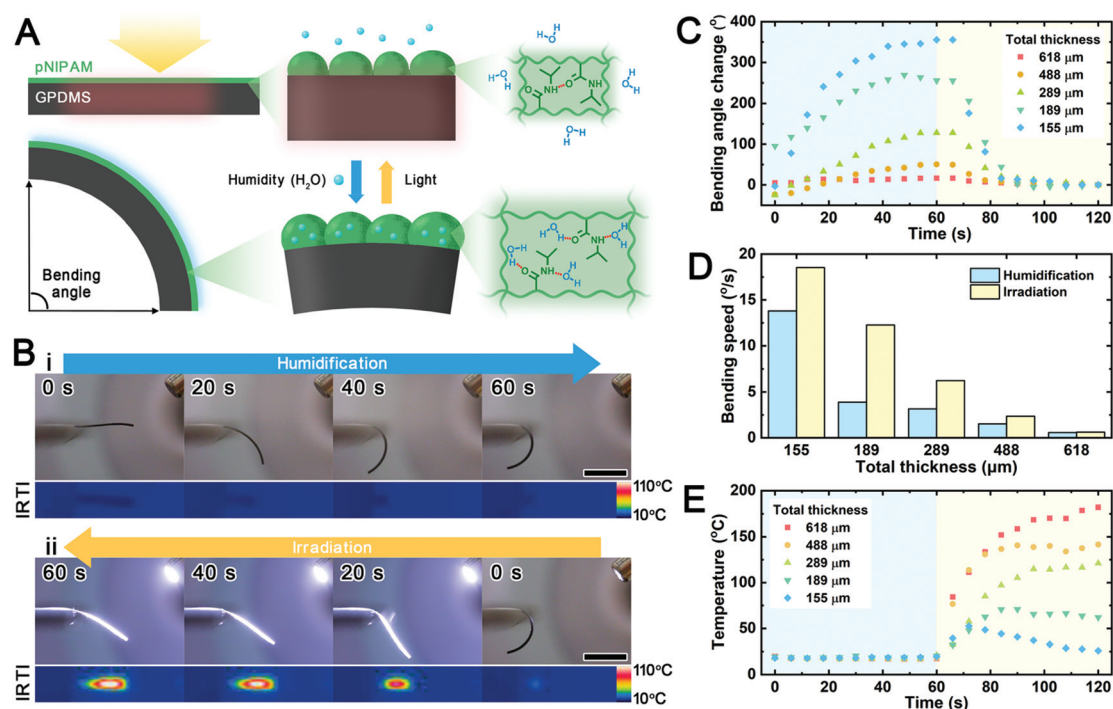
Fig. 3 Mechanism, demonstration, and characterization of stimuli-responsive behavior. (A) Schematic illustration of the pNIPAM@GPDMS actuator deformation under visible light irradiation (unbending) and humidity (bending). (B) Photograph (side view) and infrared thermal image (IRTI, top view) of the responsiveness under humidification and visible light irradiation (thickness of the actuator = 289 μm). Scale bar: 5 mm. Thermal scale bar: 10–110 °C. (C) Bending angle change of the pNIPAM@GPDMS actuator under time-varying high humidity (RH = 100%) and light irradiation (power = 400 mW). Light blue and yellow shaded regions denote high humidity and light irradiation states, respectively. (D) Bending speed of actuators with different thicknesses in the first 20 s after humidification and light irradiation. (E) Temperature profile of the pNIPAM@GPDMS actuator with different thicknesses as the actuator is first subjected to high humidity (RH = 100%) and then, after 60 s, light irradiation (power = 400 mW). Light blue and yellow shaded regions denote high humidity and light irradiation states, respectively. All the tested actuators are 10 mm long and 1 mm wide.

temperature (LCST) of 32 °C. This property leads it to transition between a swollen and a shrunken state.[33] Its volume change is even more pronounced when exposed to heat in air (Fig. S6†). As a photothermal conversion layer, the GPDMS would generate and transfer heat to the pNIPAM layer under light irradiation. Therefore, when the temperature is below the LCST of pNIPAM, the pNIPAM absorbs moisture from the environment and swells, causing the actuator to bend toward the GPDMS side. In contrast, when light causes the temperature to be higher than its LCST, pNIPAM dehydrates and shrinks. The actuator recovers to unbend or even bends towards the pNIPAM side. A selected pNIPAM@GPDMS actuator exhibits its humidity and light responsiveness as shown in Fig. 3B and Movie S1.† The original state of the actuator is straight and gradually becomes curved over the course of time when humidification begins. According to the quantitative data (Fig. 3C), the bending angle change of this actuator reaches around 153° after 60 s of humidification. The temperature of the actuator during humidification remains constant at a room temperature of 18 °C (Fig. 3E). As the visible light beam is switched on, the temperature of this actuator shoots up to about 115 °C after 36 s of light irradiation. Its morphology simultaneously returns from a curved to a flattened

shape. Several cycle tests are carried out to confirm the reproducibility of these movements (Fig. S7†). As a control group without GNP doping, the pNIPAM@PDMS actuator does not move when a light beam irradiates it after the humidifying step (Movie S2†). Thus, we can confirm the photo-thermo-motion conversion mechanism of the pNIPAM@GPDMS actuator.

Furthermore, we compared the effect of different total thicknesses, ranging from 155 to 618 μm, on the bending responses and monitored their temperature variations (Fig. 3C, D and E). This set of samples share a very similar thickness of the pNIPAM layer (14.2 ± 3 μm), but various thicknesses of the GPDMS layer (from 139 μm to 606 μm). As a passive layer, the thinner GPDMS layer will generate less resistance against bending. Therefore, we can observe that the thinner the actuator is, the larger the change in bending angle will be, under the same external stimulus conditions (Fig. 3C). We can also deduce that the thinner actuator has quicker responsiveness to changes in stimuli (Fig. 3D). Even though the thin actuator produces less heat under the same light irradiation (Fig. 3E), it still exhibits the largest change in bending angle (350°) and the fastest bending speed (17° s⁻¹) among these samples. This result indicates that the

thickness dominates the responsive performance of our pNIPAM@GPDMS system. Timoshenko's theory of a bi-material beam is proposed to predict the swelling-induced bending shape of the bilayer strips.[19,34,35] Based on its bending curvature equation, the curvature of a bilayer actuator will depend on the thickness of each layer, assuming that the Young's modulus of the material is constant during the response (Note S1†). Therefore, designing the thickness of each layer is the key to customizing the responsiveness of the actuator. Experimentally, the ratio of the hydrogel to elastomer thickness in pNIPAM@GPDMS with the best responsiveness is about 0.09. This value is much lower than other reported hydrogel-elastomer actuators so far (Table S1†). It suggests that the prepared actuator can obtain a relatively large driving force based on a thin hydrogel grafting layer. We hypothesize that this effect comes from the strong bonding brought by the BP treatment.[18,25] The high concentration of BP doping can form denser chemically binding sites at the interface of the hydrogel and elastomer.[18] A thin and strong hydrogel layer brings two benefits to the actuator: (i) the hydrogel layer with a smaller thickness can be filled with or empty water faster, enhancing the responsiveness of the actuator in air; (ii) the snakeskin-like hydrogel surface has a large gradient of stiffness with hierarchical textures leading to a low coefficient of friction, which is not easily scratched off during operation.[32] In summary, the bending and unbending of the pNIPAM@GPDMS actuator could be controlled by the humidity in air and light-induced heating. Combined with the tunable composition and geometry, soft micro-robots can be designed with different control modes and motion types.

Biomimetic soft micro-robots fabricated using the pNIPAM@GPDMS actuator

We have demonstrated the bending and unbending motions of the actuator with pNIPAM@GPDMS stripes. These demonstrated actuations can also be integrated into more sophisticated soft micro-robotic systems. Getting the robot to perform specific motions requires coordination of its geometrical features and control modes.[36] The geometry of the pNIPAM@GPDMS actuator can be tailored conveniently, and its composition can be efficiently designed by co-doping. Based on this, we fabricated a set of biomimetic micro-robots with well-designed shapes and control modes. These robots mimic some vital movements of natural creatures, such as the grabbing of a claw, the crawling of reptiles, and the jumping of spores. Here we categorize the biomimetic motions we study into directional and non-directional movements (Fig. 1).

Directional movements of pNIPAM@GPDMS micro-robots. Directional movements refer to the movements of a robot by manipulating parts or the whole robot in the same designated direction. To study such behavior, we mainly focus on the on-demand manipulation of these robots. Depending on the manipulation sequence of the robot's moving parts, we subdivided the directional motion into synchronous and asynchronous movements. Synchronous movement refers to the triggering of all the symmetrical actuators of the robot at the same

time. For example, their natural counterparts and flower petals bloom as they sense sunlight, and the flytrap senses the touch of prey and closes. These movements belong to the nastic movements of plants. To demonstrate the nastic movement by our actuator, a symmetrical petal-shaped sheet is cut out of the pNIPAM@GPDMS bilayer as an artificial flower (Fig. 4A). We placed the artificial flower on an iced platform to maintain a relatively lower temperature. The low temperature raises the relative humidity of the ambiance. Meanwhile, it can also promote the pNIPAM layer to absorb water from the surrounding air, triggering the petals to close (Fig. 4Bii and Movie S3†). Conversely, the light beam applied to the flower can generate a circular high-temperature area at the center, dehydrating the pNIPAM layer and then opening the petals synchronously (Fig. 4Bi and Movie S3†). The artificial flower responds to humidity and light, which is reminiscent of the plant's nastic movements. In addition to mimicking the nastic movements, synchronous motion can also be used in some delicate mechanical applications, such as catching and releasing objects like claws. We imitate the claws of birds to design a gripper that can be opened and closed in the presence and absence of light, respectively (Fig. 4C). During the operation, radial claws open simultaneously under symmetrical irradiation to fit the object into the claws. After the light is turned off, the claws tighten and apply pressure to grab and lift the object. Finally, a second irradiation is applied to release the object (Fig. 4D and Movie S4†). This catch-release motion remains stable after 30 cycles of repetitive testing without apparent decrease in the performance (Movie S5†). Moreover, the maximum weight that the gripper can lift is 0.565 g, which is 36 times the weight of the gripper itself (0.0156 g) (Fig. S8†). Overall, the artificial flower and gripper designs achieve the synchronized radial movement of the soft robot through radially symmetric geometries and coaxial light irradiation regions. From these demonstrations, the GPDMS layer shows not only its photothermal properties but also its hydrophobicity and elasticity, maintaining the overall robotic structure to be sturdy. Even after being out of water or humid atmosphere for a long time, the robotic structure will not collapse due to excessive dehydration. Hence, the operation can be performed without being confined to the water environment, and the humidity can be taken as a stimulus to control the actuator movement.

Compared to the symmetry obtained by synchronous movement, the asymmetry obtained by asynchronous movement makes the robot impart additional flexibility in the choice of motion direction, especially in 'walking' motion. A robot must actuate different moving parts asynchronously to complete a set of motions to walk one step forward. This set of motions is then repeated over and over again to keep the robot moving in the same direction as a whole. In this study, a quadruped robot is fabricated by mimicking quadruped reptiles (Fig. 4E). The quadruped robot's forelegs, body, and hind legs can be separately actuated by local irradiation. When the beam is swept from right to left, it sequentially heats the forelegs, body, and hind legs of the robot, generating spatially and tem-
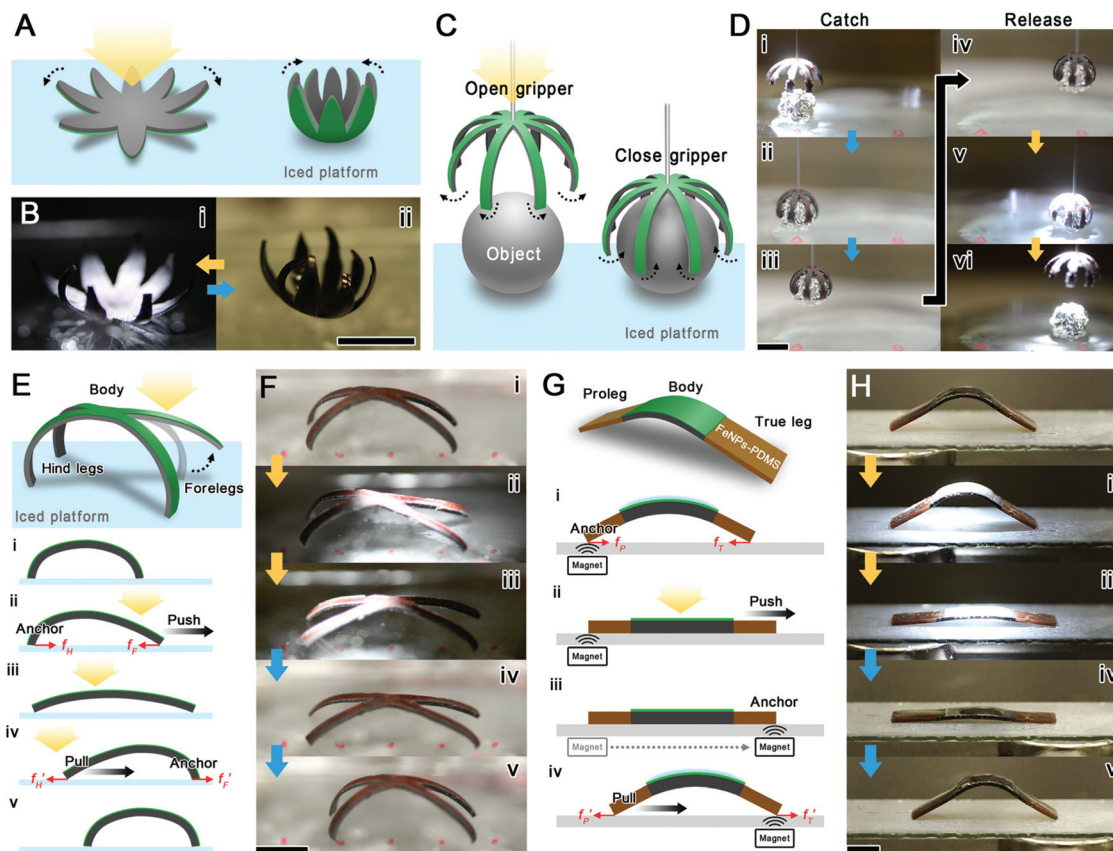
Fig. 4 Directional movements of the pNIPAM@GPDMS actuator *via* local irradiation. (A) Schematic illustration of the nastic movement of the artificial flower and (B) photographs of its petals opening in bright light and closing when the light fades. (C) Schematic illustration of the gripper and (D) snapshots when it performs catch and release by light control. (E) Schematic illustration of a quadruped robot (the frictional forces on the hind legs are defined as f_H or f_H'; the frictional forces on the forelegs are defined as f_F or f_F') and (F) snapshots when it performs crawling movement under sequential light irradiation. (G) Schematic illustration of a caterpillar robot (the frictional forces on the proleg are defined as f_P or f_P'; the frictional forces on the true leg are defined as f_T or f_T') and (H) snapshots of the robot performing inching by alternating the conditions of local humidity, light irradiation, and magnetism. The power of the light beam applied in the cases here is 400 mW and the magnetic field intensity is 88 mT. Scale bars: 5 mm.

porally asynchronous deformations. This asynchronous deformation, in turn, provides the robot with a pair of opposite frictional forces (Fig. 4Eii and Eiv). The legs with greater curvature will have greater maximum static friction than those with less curvature due to their different friction coefficients. For example, in Fig. 4Eii, f_H is the static friction and f_F is the sliding friction, so the hind legs would anchor and push the forelegs forward. Inversely, in Fig. 4Eiv, f_F' is the static friction while f_H' is the sliding friction. Hence, the forelegs would anchor and pull the hind legs back. The consequence of this series of frictions allows the robot to crawl forward (Fig. 4F and Movie S6†). Nevertheless, the moving direction of this quadruped robot depends not only on the light sweeping direction but also on the state of its contact surface. An uneven contact surface roughness would make its next movement difficult to predict. In light-only control mode, some of the movements are ineffective. Fortunately, this co-doping system has high compatibility with multiple functionalized dopants. The design of a robot with multiple control modes

can ensure every motion is more predictable and controllable. We designed a caterpillar robot by doping GNPs and FeNPs at different sites to combine magnetic control with light control (Fig. 4G and S9†). Typically, the body is still composed of pNIPAM@GPDMS, while the front and rear ends consist of magnetic FeNP doped PDMS (FeNP-PDMS). Combined with the magnetic attraction, the static frictional force between the legs and platform would be largely enhanced. Hence, the additional magnetic ends can function similarly as the proleg and true leg of a caterpillar. These magnetic ends ensure effective anchoring of legs on the platform at each step, so repeated light irradiation and humidification are only needed on the body part. In this way, the robot could move more steadily without the adverse effects of variable friction coefficients on the platform (Fig. 4H and Movie S7†). All in all, the asynchronous motion is realized in two separate ways: local light manipulation and multiple control mode. These two control methods are expected to improve the precision of the manipulation and allow it to perform more sophisticated movements.

Non-directional (random) movements of pNIPAM@GPDMS micro-robots

Except for the active directional movement, many small creatures move passively in nature, such as the dispersal of spores and microorganisms. They are less controllable and depend more on the changes in the surrounding environment. These movements are presented as disorderly and random movements, which are also known as non-directional movements. Among the natural counterparts, the *Equisetum* plants (horsetails) can spread their spores with the assistance of the humid-

ity cycle of the environment.[37] These spores have four flexible ribbon-like appendages called elaters. The elaters are humidity-responsive, coil around the main spore body in humid air, and deploy as they dry. Elaters have been proven to help disperse the spores *via* walking and jumping driven by humidity cycles.[37] To mimic the *Equisetum* spore, we designed a miniaturized pNIPAM@GPDMS robot (spore robot) and demonstrated the non-directional movement of a soft micro-robot (Fig. 5A and S10A†). Instead of humidity cycles, we used the humidity-light cycle to actuate the movement of the spore robots. The elaters of the robots regularly open and close in
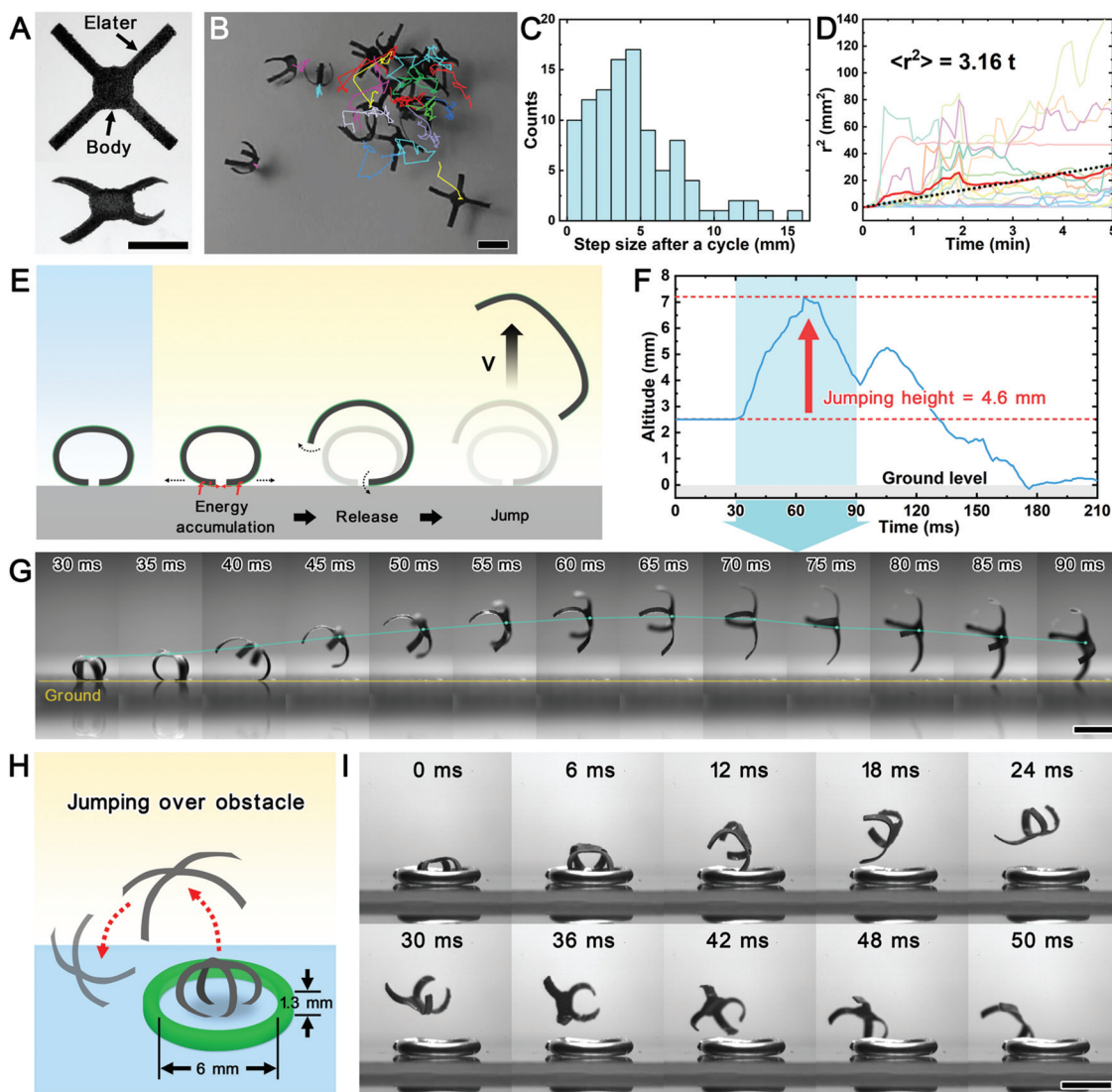

Fig. 5 Non-directional movements of the pNIPAM@GPDMS actuator *via* large-area irradiation. (A) Photographs of the two states of the spore robot (upper: unbent state; bottom: bent state). Scale bar: 5 mm. (B) Motion of spore robot swarm under a succession of six humidity-light cycles (100% RH for 10 s and 3000 lux for 60 s, T_{cycle} = 70 s). Scale bar: 5 mm. (C) Distribution of step sizes during a trajectory. The step size is defined as the distance between positions at the beginning of each cycle. The average step size here is 4.5 mm. (D) Travelled distance as a function of time for several trajectories. The red curve is the average of all trajectories over time and the dotted line shows diffusion with $\langle r^2 \rangle = 4dt$. (E) Jumping mechanism of a spore robot (only two elaters are drawn). Elaters can be stuck by friction. The released elaters, when stresses overcome static friction, are drawn with dashes. (F) The altitude of the spore robot in the jump. Blue shaded regions denote a set of rising and falling. (G) Sequential images show the jumping of a spore robot on a glass surface under light irradiation. The time interval between each snapshot is 5 ms. Scale bar: 5 mm. (H) Schematic illustration and (I) sequential images showing a spore robot jumps over a ring-shaped obstacle. Scale bar: 5 mm.

response to repetitive humidity-light cycles (Fig. 5B and Movie S8†). The location of the center of mass oscillates after one cycle but does not revert to its former position. The distance between the former and later positions is the step walked by the robot. Although the amplitude of these walks fluctuates, we can still calculate the average amplitude of steps from the distribution of step sizes during a trajectory (Fig. 5C), which is 4.5 mm in our case. The non-directional movements are caused by kinetic friction incurred as the elaters slide on the ground or entangle with each other during the opening–closing cycles. The change in kinetic friction is irreversible because the site of static contact is displaced in each step of the robot's walking. The variability in the direction of these steps comes from the changes in the contact points of the robot's four elaters during their opening–closing cycles. The trajectory tracking of many spore robots shows that the robots disperse in the two-dimensional (2-D) plane (Fig. 5B). Each spore's average traveling distance r follows a 2-D Brownian motion (diffusion) law $\langle r^2 \rangle = 4dt$, where d is the 2-D diffusion coefficient and t is the time elapsed from a starting position. The average graph (the red graph in Fig. 5D) is calculated over a number of trajectories and starting points. Then the value of the diffusion coefficient of spore robots is estimated to be around 0.79 mm^2 min^{-1} ($\approx 1.32 \times 10^{-4}$ cm^2 s^{-1}). Besides 2-D random walks, incidental jumping among individuals also promotes the non-directional movement of the micro-robot swarm.

When drying from a hydrated state under light irradiation, some spore robots are observed to jump out of the ground suddenly (Movie S9†). The robot leaves the ground at a speed of approximately 0.27 m s^{-1} and reaches an elevation of up to 4.6 mm (Fig. 5F and G). This altitude is almost twice the original height of the robot (2.5 mm). By examining the snapshots in the slow-motion video, we hypothesize that the elaters can be temporarily stuck by static friction localized between the elaters or elater and the ground during their opening process (Fig. 5E). This friction also allows the elaters to store elastic energy. Once the accumulated elastic forces become larger than the static friction, the energy will be released. In this process, one elater is still in contact with the ground and pushes the body upwards. This elater behaves as a compressed spring releasing its energy. The elasticity of the robot is attributed to the elastomer in the bilayer. Meanwhile, the thickness of the spore robot can reach 155 μm, and laser cutting allows a 2-D resolution of 0.7 mm (Fig. S10B†). The weight of each resulting spore robot is only 2.75 mg (±0.25 mg). The elasticity of the material and its lightweight created by the processing method enable the spore robot to overcome gravity and jump off the ground, even over obstacles (Fig. 5H, I, and Movie S10†). Overall, as the robot scale gets smaller, the degree of motion control becomes limited by the inability to control environmental factors, such as temperature, light, humidity, and other external stimuli. These stimuli would cause the non-directional movements of the robot. Therefore, understanding the robot's passive non-directional movements can help us to develop environmentally responsive miniaturized robots.

Conclusions

In conclusion, we have developed a hydrogel-elastomer actuator based on our co-doping method that combines the surface treatment and functionalization steps into only one step, avoiding intricate processes or excess reagent consumption in conventional approaches. The proposed actuator material can be customized with tunable thicknesses of the bilayer and multiple doping combinations. We have demonstrated this concept by designing the thermo-responsive hydrogel pNIPAM with the photothermal elastomer GPDMS. The prepared pNIPAM@GPDMS actuator responds to changes in humidity and light. A series of pNIPAM@GPDMS micro-robots have been developed to perform versatile biomimetic motions, including directional and non-directional movements. These demonstrations not only suggest the feasibility of the actuator but also deepen the understanding of biomimetic motions achieved by hydrogel-elastomer actuators. We believe that this strategy of stimuli-responsive micro-actuator preparation, as well as its display of versatile biomimetic motions, will inspire the design and application of novel soft micro-robots in the fields of self-locomotive robots in environmental monitoring and drug delivery robots in biomedical engineering.

Author contributions

Y. Pan proposed the idea, developed and conducted the majority of the experiments, and prepared the original draft. L. H. Lee helped with the experiment development and data collection. Z. Yang, S. U. Hassan and H. C. Shum reviewed and edited the original draft. H. C. Shum supervised the project. All authors read and approved the final manuscript.

Conflicts of interest

There are no conflicts to declare.

Acknowledgements

Notes and references

1 D. Rus and M. T. Tolley, *Nature*, 2015, **521**, 467.
2 M. Ilami, H. Bagheri, R. Ahmed, E. O. Skowronek and H. Marvi, *Adv. Mater.*, 2021, **33**, 2003139.
3 P. Wang, M. A. R. Al Azad, X. Yang, P. R. Martelli, K. Y. Cheung, J. Shi and Y. Shen, *Proc. Natl. Acad. Sci. U. S. A.*, 2021, **118**, e2024329118.
4 Q. Zhao, Y. Wang, H. Cui and X. Du, *J. Mater. Chem. C*, 2019, **7**, 6493.
5 S. Coyle, C. Majidi, P. LeDuc and K. J. Hsia, *Extreme Mech. Lett.*, 2018, **22**, 51.
6 V. Kumar, U. H. Ko, Y. Zhou, J. Hoque, G. Arya and S. Varghese, *Adv. Intell. Syst.*, 2021, **3**, 2100005.
7 H. Cui, Q. Zhao, Y. Wang and X. Du, *Chem. – Asian J*, 2019, **14**, 2369.
8 H. Lu, Y. Hong, Y. Yang, Z. Yang and Y. Shen, *Adv. Sci.*, 2020, **7**, 2000069.
9 H. Kim, S.-k. Ahn, D. M. Mackie, J. Kwon, S. H. Kim, C. Choi, Y. H. Moon, H. B. Lee and S. H. Ko, *Mater. Today*, 2020, **41**, 243.
10 S. J. Jeon, A. W. Hauser and R. C. Hayward, *Acc. Chem. Res.*, 2017, **50**, 161.
11 O. M. Wani, H. Zeng and A. Priimagi, *Nat. Commun.*, 2017, **8**, 15546.
12 X. Le, W. Lu, J. Zhang and T. Chen, *Adv. Sci.*, 2019, **6**, 1801584.
13 K. Sano, Y. Ishida and T. Aida, *Angew. Chem., Int. Ed.*, 2018, **57**, 2532.
14 F. Fu, L. Shang, Z. Chen, Y. Yu and Y. Zhao, *Sci. Robot.*, 2018, **3**, eaar8580.
15 X. Liu, J. Liu, S. Lin and X. Zhao, *Mater. Today*, 2020, **36**, 102.
16 Y. Lee, W. J. Song and J. Y. Sun, *Mater. Today Phys.*, 2020, **15**, 100258.
17 Z. Zhang, Z. Chen, Y. Wang, J. Chi, Y. Wang and Y. Zhao, *Small Methods*, 2019, **3**, 1900519.
18 H. Yuk, T. Zhang, G. A. Parada, X. Liu and X. Zhao, *Nat. Commun.*, 2016, **7**, 12028.
19 A. M. Hubbard, W. Cui, Y. Huang, R. Takahashi, M. D. Dickey, J. Genzer, D. R. King and J. P. Gong, *Matter*, 2019, **1**, 674.
20 H. Li, Y. Liang, G. Gao, S. Wei, Y. Jian, X. Le, W. Lu, Q. Liu, J. Zhang and T. Chen, *Chem. Eng. J.*, 2021, **415**, 128988.
21 C. Yang and Z. Suo, *Nat. Rev. Mater.*, 2018, **3**, 125.
22 S. Vanaei, M. S. Parizi, S. Vanaei, F. Salemizadehparizi and H. R. Vanaei, *Eng. Regen.*, 2021, **2**, 1.
23 X. Li, X. Cai, Y. Gao and M. J. Serpe, *J. Mater. Chem. B*, 2017, **5**, 2804.
24 D. Wirthl, R. Pichler, M. Drack, G. Kettlguber, R. Moser, R. Gerstmayr, F. Hartmann, E. Bradt, R. Kaltseis, C. M. Siket, S. E. Schausberger, S. Hild, S. Bauer and M. Kaltenbrunner, *Sci. Adv.*, 2017, **3**, e1700053.
25 H. Lin, S. Ma, B. Yu, X. Pei, M. Cai, Z. Zheng, F. Zhou and W. Liu, *Chem. Mater.*, 2019, **31**, 9504.
26 Y. Hayashi, *Chem. Sci.*, 2016, **7**, 866.
27 H. Geng, K. Zhou, J. Zhou, H. Ma, C. Lv, C. Li, Z. Xu and L. Qu, *Angew. Chem., Int. Ed.*, 2018, **57**, 15435.
28 Y. Yu, H. Yuk, G. A. Parada, Y. Wu, X. Liu, C. S. Nabzdyk, K. Youcef-Toumi, J. Zang and X. Zhao, *Adv. Mater.*, 2019, **31**, 1807101.
29 S. Liu, X. Pan and H. Liu, *Angew. Chem., Int. Ed.*, 2020, **59**, 5890.
30 Y. Yang, Y. Liu and Y. Shen, *Adv. Funct. Mater.*, 2020, **30**, 1910172.
31 Y. Yang and Y. Shen, *Adv. Opt. Mater.*, 2021, **9**, 2100035.
32 M. Wang, S. K. Ghosh, C. M. Stafford, A. K. Blevins, S. Huang, J. Martinez, R. Long, C. N. Bowman, J. P. Killgore, M. Zou and Y. Ding, *ACS Appl. Mater. Interfaces*, 2020, **12**, 57450.
33 L. Tang, L. Wang, X. Yang, Y. Feng, Y. Li and W. Feng, *Prog. Mater. Sci.*, 2021, **115**, 100702.
34 Y. Wu, X. Hao, R. Xiao, J. Lin, Z. L. Wu, J. Yin and J. Qian, *Acta Mech. Solida Sin.*, 2019, **32**, 652.
35 S. Timoshenko, *J. Opt. Soc. Am.*, 1925, **11**, 22.
36 S. Persiani, *Biomimetics of Motion: Nature-Inspired Parameters and Schemes for Kinetic Design*, Springer, 2018.
37 P. Marmottant, A. Ponomarenko and D. Bienaime, *Proc. Biol. Sci.*, 2013, **280**, 20131465.